

Probing Electric Field Distributions in the Double Layer of a Single-Crystal Electrode with Angstrom Spatial Resolution using Raman Spectroscopy

Bao-Ying Wen, Jia-Sheng Lin, Yue-Jiao Zhang, Petar M. Radjenovic, Xia-Guang Zhang,*
Zhong-Qun Tian, and Jian-Feng Li*

 Cite This: *J. Am. Chem. Soc.* 2020, 142, 11698–11702

 Read Online

ACCESS |

 Metrics & More

 Article Recommendations

 Supporting Information

ABSTRACT: The electrical double layer (EDL) is the extremely important interfacial region involved in many electrochemical reactions, and it is the subject of significant study in electrochemistry and surface science. However, the direct measurement of interfacial electric fields in the EDL is challenging. In this work, both electrochemical resonant Raman spectroscopy and theoretical calculations were used to study electric field distributions in the EDL of an atomically flat single-crystal Au(111) electrode with self-assembled monolayer molecular films. This was achieved using a series of redox-active molecules containing the 4,4'-bipyridinium moiety as a Raman marker that were located at different precisely controlled distances away from the electrode surface. It was found that the electric field and the dipole moment of the probe molecule both directly affected its Raman signal intensity, which in turn could be used to map the electric field distribution at the interface. Also, by variation of the electrolyte anion concentration, the Raman intensity was found to decrease when the electric field strength increased. Moreover, the distance between adjacent Raman markers was ~ 2.1 Å. Thus, angstrom-level spatial resolution in the mapping of electric field distributions at the electrode–electrolyte interface was realized. These results directly evidence the EDL structure, bridging the gap between the theoretical and experimental understandings of the interface.

Many significant electrochemical reactions happen in the electrical double layer (EDL),^{1–6} at the electrode–electrolyte interface. The most commonly used model of the electrochemical interface was modified by Bockris et al. on the basis of the Gouy–Chapman–Stern model.^{7–9} The EDL contains two regions: the Stern layer and the diffuse layer. Starting at the electrode surface and moving out into the bulk electrolyte, the electric potential first decreases linearly (Stern layer) and then exponentially (diffuse layer). The EDL structure influences the electric potential distribution within these layers, which can affect the electrochemical reaction mechanisms and rates. Hence, elucidating EDL structures and electric field distributions is an important but challenging fundamental endeavor.

Recently, techniques such as cyclic voltammetry and infrared, Raman, and X-ray absorption spectroscopies have been applied to study interfacial layers and the EDL structure.^{10–19} For example, Gooding et al.¹² used cyclic voltammograms (CVs) of self-assembled monolayers (SAMs) of ferrocene on electrode surfaces to measure the formal potential of surface ferrocene. They then calculated the interfacial potential distribution of the electrical double layer using the method proposed by Smith and White.¹⁵ Harris et al. used surface-enhanced Raman spectroscopy to measure the Stark tuning rates of nitrile-terminated SAMs to predict interfacial electric fields.¹¹ Despite these significant advances, those techniques rely upon SAMs with unstable thicknesses and roughened Ag electrode surfaces, which structurally vary

and thus cannot accurately measure electric fields with angstrom resolution.

In the present work, electrochemical resonant Raman spectroscopy was used to measure the electric field distribution within the double layer at the electrode–electrolyte interface of an atomically flat single-crystal Au(111) electrode coated with different viologen-based SAMs (Figure 1a). To maintain uniform SAM thicknesses, seven different viologen molecules with different alkyl chain lengths but a total length of 16 carbon atoms (Figure 1b) were synthesized and used to construct the SAMs. The seven viologen molecules are labeled HS- $nV(16 - n)$. From the mercapto surface anchoring group, the alkyl chain lengths (n and $16 - n$) were varied to change the position of the 4,4'-bipyridinium group (V), used as a Raman marker, within the overall molecule. Thus, the distance between the Raman marker and the electrode surface could be precisely controlled and changed. By variation of the distance of the marker group from the surface and measurement of changes in its Raman signal intensity, the changes in the electric field distribution within the double layer were observed with angstrom spatial resolution. By measurement and

Received: May 13, 2020

Published: June 17, 2020



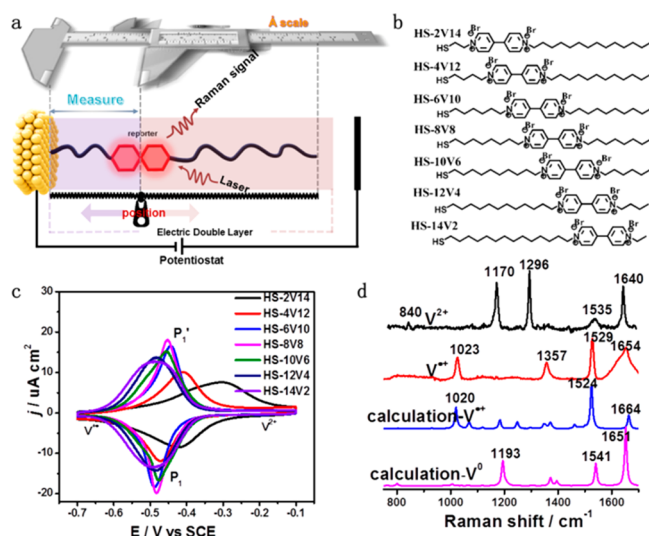


Figure 1. (a) Schematic diagram of the “molecular ruler”. (b) Chemical structural formulas of the seven viologen molecules. (c) CVs of the seven different viologen molecular SAMs on Au(111) in 100 mmol/L NaClO₄ at pH 7–8 (scan rate = 50 mV/s). (d) Experimental and calculated Raman spectra of viologen HS-6V10 in different states.

simulation of the signal intensities of the Raman marker at different electrolyte concentrations, the effect of changes in the double layer electric field distributions could be effectively imaged, providing important information about the EDL structure.

The redox-active viologen moiety has three distinct oxidation states and two successive one-electron redox processes: $V^{2+} \rightleftharpoons V^{+\bullet}$ and $V^{+\bullet} \rightleftharpoons V^0$.²⁰ Figure 1c shows typical CVs of the various viologen SAMs on a Au(111) electrode between -0.2 and -0.65 V vs SCE in 100 mmol/L NaClO₄. Clear redox current peaks (P_1/P_1') are visible for all of the SAMs within this potential region and are assigned to the first redox process ($V^{2+} \rightleftharpoons V^{+\bullet}$), where the viologen molecules are completely converted to $V^{+\bullet}$ at -0.7 V vs SCE. CVs were also used to calculate the SAM surface coverage (Table S1), corresponding to a surface coverage of $(3.5 \pm 1) \times 10^{-10}$ mol/cm², which is consistent with literature reports.^{21–24} However, it is significantly lower than the surface coverage of densely packed alkanethiol SAMs ($\sim 8 \times 10^{-10}$ mol/cm²).²⁵ Therefore, electrolyte ions will likely be able to penetrate into the SAMs and form ion pairs with viologen moieties, thereby influencing electric fields in the double layer. The ion-pair concentration will differ with changes in surface coverage, which can change the nature of the double layer.

The experimental/calculated Raman spectra of different viologen oxidation states are presented in Figures 1d and S2. Of the three states, the $V^{+\bullet}$ radical cation, unlike the other two states, is stable and can produce strong resonant Raman spectra under 638 nm laser illumination.²¹ Figure 2a shows the resonant Raman spectra of the seven viologen SAMs on Au(111). All of the spectra have been normalized to the surface coverage. In all of the spectra, four characteristic Raman bands attributed to $V^{+\bullet}$ are visible at 1028, 1359, 1529, and 1656 cm⁻¹.²¹ The strongest $V^{+\bullet}$ band at 1529 cm⁻¹ is assigned to in-plane C–C stretching and C–H bending in the 4,4'-bipyridinium group. Differences in the normalized Raman intensities of the 1529 cm⁻¹ band of the respective SAMs can be used to study electric field distribution at different

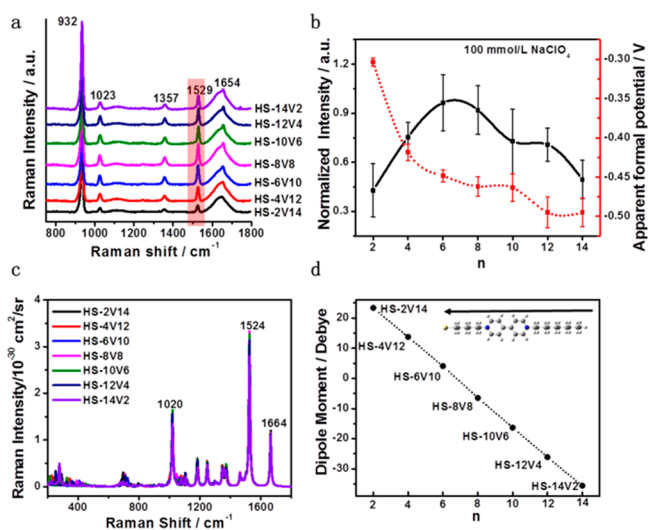


Figure 2. (a) Resonant Raman spectra of the seven viologen SAMs on Au(111) in 100 mmol/L NaClO₄ (pH 7–8) at -0.7 V vs SCE. The band at 932 cm⁻¹ results from ClO₄⁻ ions. (b) Normalized Raman intensities of the 1529 cm⁻¹ peak (black line) at -0.7 V vs SCE and the apparent formal oxidation potentials (red dashed line). (c) Simulated Raman spectra of the $V^{+\bullet}$ state. (d) Dipole moments (in Debyes) of HS- n V(16 - n)⁺. The positive direction is defined as $V^{+\bullet}$ toward the Au(111) electrode.

positions in the double layer. Figure 2b (black line) shows the normalized Raman intensity of the 1529 cm⁻¹ peak as a function of the alkyl chain length n . The normalized Raman intensity first increases then decreases as n increases, reaching a maximum at HS-6V10. Additionally, the formal oxidation potentials of the viologen molecules (Figure 1c) are included in Figure 2b (red dotted line). With increasing distance from the electrode surface, the potential drops sharply and then slowly, and the change in oxidation potential is roughly consistent with the Raman intensity result that the turning point occurred at HS-6V10. On the basis of the literature,¹² changes in oxidation potential due to the changing distance of the redox-active viologen marker group from the electrode surface may be related to the EDL structure. The Raman intensity of the 1529 cm⁻¹ peak is also affected by the electric fields in the double layer and increases sharply when $V^{+\bullet}$ moves out of the Stern layer. However, it does not continue to rise and begins to decrease. Intrinsic structural properties and ion-pair formation may contribute to this decrease in Raman intensity. In Figures 2c,d, S3, and S4, the intrinsic Raman intensities of the seven HS- n V(16 - n)⁺ molecules are fundamentally the same, while their dipole moments are different because of the different charge distributions, which influence the Raman intensity in the electrochemical environment.

Because of the hydrophobic nature of $V^{+\bullet}$, polarizing the electrode surface will result in the formation of an ion-pair layer between $V^{+\bullet}$ and the electrolyte anion, producing an induced electric field in the SAMs. As discussed previously, the ion penetration into the SAMs is dependent on the surface coverage and anion concentration in the electrolyte, while the Raman intensity of $V^{+\bullet}$ spectral bands is influenced by the induced electric field. For these reasons, the Raman intensities for all of the molecules were calculated under exposure to different electric dipole fields at -0.7 V vs SCE (Tables S2–S8). Clear Raman intensity changes occur as a result of

changes in the electric dipole field, and the degree of change differs among the molecules, suggesting that the sequence of Raman intensity for the seven molecules would be changed in different induced electric fields.

To verify the accuracy of the above results, the concentration of ion pairs was adjusted by varying the NaClO_4 electrolyte concentration to study the effect of the induced electric field on the spectral band intensities of the Raman markers in the different SAMs. In Figure 3a,b, the

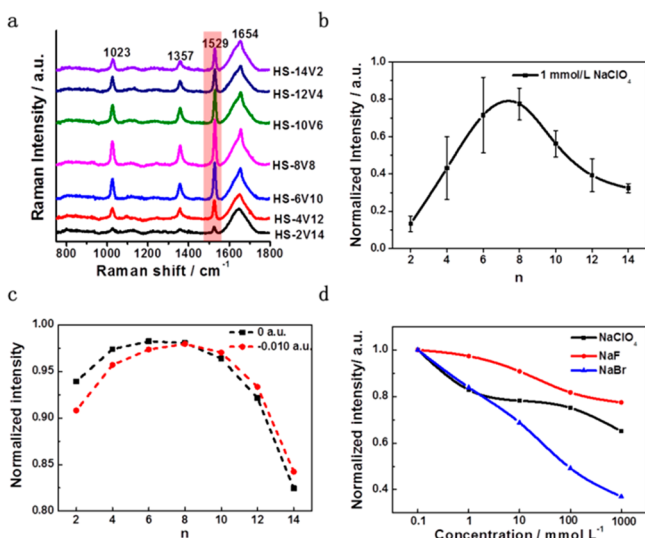


Figure 3. (a) Resonant Raman spectra of seven $\text{V}^{+\bullet}$ SAMs on Au(111) in 1 mmol/L NaClO_4 (pH 7–8) at -0.7 V vs SCE. (b) Normalized Raman intensities of the 1529 cm^{-1} peak. Error bars represent experimental data results from different single crystals. (c) Calculated Raman intensities of the 1529 cm^{-1} peak for the seven molecules exposed to 0 au and -0.010 au dipole electric fields. Intensities are given relative to HS-8V8. (d) Concentration dependence of the 1529 cm^{-1} intensities for HS-6V10 in NaClO_4 , NaF, and NaBr.

Raman intensity using 1 mmol/L NaClO_4 is consistent with the 100 mmol/L results in Figure 2b; however, the amplitude of the curve differs. Changing the NaClO_4 concentration appears to change the double layer structure, causing the maximum Raman signal to shift from $n = 6$ (Figure 2b) to $n = 8$ (Figure 3b). Furthermore, the experimental results agree well with the trend in the calculated results in Figure 3c, which shows a maximum Raman intensity shift to HS-8V8 upon exposure to other dipole electric fields. Moreover, different electrolytes, such as NaF, also supported this observation (Figure S5).

These results show that the electric field has a major influence on the Raman intensity. Thus, the effect of the electric field was studied by carefully changing the ion concentration of the supporting electrolyte with one type of viologen molecule (HS-6V10) on the Au(111) electrode. The Raman intensity of the 1529 cm^{-1} peak (normalized to 0.1 mmol/L) clearly decreases with increasing NaClO_4 concentration (Figure S6). The same trend was observed for the HS-12V4 SAM (Figure S7) as for HS-6V10. This occurs because increasing the electrolyte concentration induces stronger electric fields in the double layer, which hinders the vibration of molecules, leading to the Raman intensity decreases.

Furthermore, the electrolyte anion was also varied using NaF and NaBr (Figures S8–S10). Because of the differences in

ionic volume and adsorption energy of the anions, the ion-pair ratio differs between electrolytes. Figure 3d shows the normalized Raman intensity for HS-6V10 with different anions plotted against concentration. These results confirm the above conclusion that the electric field and Raman intensity are inversely proportional. Another interesting phenomenon in Figure 3d is the signal intensity drop, which is in the order $\Delta I_{\text{Br}^-} > \Delta I_{\text{ClO}_4^-} > \Delta I_{\text{F}^-}$. This may be due to differences in the penetration depths of the anions into the SAMs, as the water molecules in the anion hydration shell need to be removed and different anions have different hydration energies. According to the previous reports,^{26–28} the Gibbs free energies of hydration are arranged in the following order: $\Delta_{\text{hyd}}G_{\text{Br}^-}$ (-315 kJ/mol) $>$ $\Delta_{\text{hyd}}G_{\text{ClO}_4^-}$ (-430 kJ/mol) $>$ $\Delta_{\text{hyd}}G_{\text{F}^-}$ (-465 kJ/mol).²⁷ These values match the observed experimental trend, with F^- being the least effective anion at penetrating the SAM because it has the largest hydration energy; thus, it has the smallest impact on the double layer electric field, resulting in the smallest change in Raman intensity compared with the other anions.

Additionally, on the basis of the above results, we simulated the electron density distribution (n_e) of the $\text{V}^{+\bullet}$ Raman marker group at different positions in the double layer (Figure 4a).

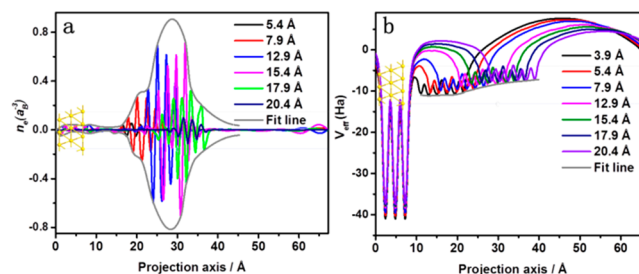


Figure 4. (a) Distribution of electron density difference (n_e) projections and (b) effective potential (V_{eff}) of the signal marker group as it is gradually moved farther away from the Au(111) surface at -0.7 V vs SCE. The gray lines in (a) and (b) are fits of n_e and V_{eff} , respectively.

The largest n_e distribution of $\text{V}^{+\bullet}$ is equal for sites of HS-6V10 and HS-8V8. Figure 4b shows the effective potential of the Raman marker group without the induced electric field. The potential is steady near the Au(111) surface and then decreases, which conforms to the EDL theory. These results suggest that the Raman intensity is influenced by synergistic effects involving the applied potential and induced electric field dictated by the electrolyte concentration. The Raman intensity of one marker group provides unambiguous evidence regarding the interaction between the applied potential and the induced electric field and maps the n_e distribution in the double layer.

In summary, SAMs composed of probe molecules were constructed on the Au(111) electrode interface, and resonant Raman spectroscopy was effectively used to detect electric field distributions in the electric double layer. This was achieved by precisely varying the distance of the Raman marker (4',4'-bipyridinium) from the surface of the electrode. Additionally, the concentration of the supporting electrolyte was also varied to determine the effect of changing the strength of the electric field, and we found that the electric field and Raman intensity of the marker were inversely proportional. Thus, we have elucidated important interfacial phenomena that significantly contribute to our understanding of the electric double layer.

■ ASSOCIATED CONTENT

SI Supporting Information

The Supporting Information is available free of charge at <https://pubs.acs.org/doi/10.1021/jacs.0c05162>.

Experimental and Computational Section, schematic illustration of the spectroelectrochemical cell, Raman spectra of HS-6V10 in different states, dipole vectors of seven molecules, Raman spectra of seven molecules in NaF, Raman spectra of HS-6V10 and HS-12V4 in different concentrations of NaClO₄, Raman spectra and CVs of HS-6V10 at different concentrations of NaF and NaBr (PDF)

■ AUTHOR INFORMATION

Corresponding Authors

Jian-Feng Li – State Key Laboratory of Physical Chemistry of Solid Surfaces, iChEM, College of Chemistry and Chemical Engineering, College of Energy, Xiamen University, Xiamen 361005, China; orcid.org/0000-0003-1598-6856; Email: Li@xmu.edu.cn

Xia-Guang Zhang – Key Laboratory of Green Chemical Media and Reactions, Ministry of Education, Collaborative Innovation Center of Henan Province for Green Manufacturing of Fine Chemicals, School of Chemistry and Chemical Engineering, Henan Normal University, Xinxiang 453007, China; orcid.org/0000-0002-9223-0852; Email: zhangxiaguang@htu.edu.cn

Authors

Bao-Ying Wen – State Key Laboratory of Physical Chemistry of Solid Surfaces, iChEM, College of Chemistry and Chemical Engineering, College of Energy, Xiamen University, Xiamen 361005, China

Jia-Sheng Lin – State Key Laboratory of Physical Chemistry of Solid Surfaces, iChEM, College of Chemistry and Chemical Engineering, College of Energy, Xiamen University, Xiamen 361005, China

Yue-Jiao Zhang – State Key Laboratory of Physical Chemistry of Solid Surfaces, iChEM, College of Chemistry and Chemical Engineering, College of Energy, Xiamen University, Xiamen 361005, China

Petar M. Radjenovic – State Key Laboratory of Physical Chemistry of Solid Surfaces, iChEM, College of Chemistry and Chemical Engineering, College of Energy, Xiamen University, Xiamen 361005, China

Zhong-Qun Tian – State Key Laboratory of Physical Chemistry of Solid Surfaces, iChEM, College of Chemistry and Chemical Engineering, College of Energy, Xiamen University, Xiamen 361005, China; orcid.org/0000-0002-9775-8189

Complete contact information is available at: <https://pubs.acs.org/doi/10.1021/jacs.0c05162>

Notes

The authors declare no competing financial interest.

■ ACKNOWLEDGMENTS

This work was financially supported by the National Natural Science Foundation of China (21925404 and 21775127), the National Key Research and Development Program of China (2019YFA0705400 and 2019YFD0901100), and the Fundamental Research Funds for the Central Universities (20720190044).

■ REFERENCES

- (1) Bard, A. J.; Faulkner, L. R. *Electrochemical Methods: Fundamentals and Applications*, 2nd ed.; John Wiley & Sons: New York, 2001.
- (2) Oleinick, A.; Svir, I.; Amatore, C. A few key theoretical issues of importance in modern molecular electrochemistry. *Curr. Opin. Electrochem.* **2019**, *13*, 33–39.
- (3) Wang, Q.; Cha, C. S.; Lu, J. T.; Zhuang, L. The electrochemistry of “solid/water” interfaces involved in PEM-H₂O reactors Part I. the “Pt/Water” interfaces. *Phys. Chem. Chem. Phys.* **2009**, *11*, 679–687.
- (4) Ledezma-Yanez, I.; Wallace, W. D. Z.; Sebastian-Pascual, P.; Climent, V.; Feliu, J. M.; Koper, M. T. M. Interfacial water reorganization as a pH-dependent descriptor of the hydrogen evolution rate on platinum electrodes. *Nat. Energy* **2017**, *2*, 17031.
- (5) Ahmed, M.; Attard, G. A.; Wright, E.; Sharman, J. Methanol and formic acid electrooxidation on nafion modified Pd/Pt{111}: the role of anion specific adsorption in electrocatalytic activity. *Catal. Today* **2013**, *202*, 128–134.
- (6) Hoang, T. T. H.; Verma, S.; Ma, S.; Fister, T. T.; Timoshenko, J.; Frenkel, A. I.; Kenis, P. J. A.; Gewirth, A. A. Nanoporous copper–silver alloys by additive-controlled electrodeposition for the selective electroreduction of CO₂ to ethylene and ethanol. *J. Am. Chem. Soc.* **2018**, *140*, 5791–5797.
- (7) Parsons, R. The electrical double layer: recent experimental and theoretical developments. *Chem. Rev.* **1990**, *90*, 813–826.
- (8) Gurney, W. R. Theory of electrical double layers in adsorbed films. *Phys. Rev.* **1935**, *47*, 479–482.
- (9) Bockris, J. O.; Devanathan, M. A. V.; Muller, K. On the structure of charged interfaces. *Electrochemistry* **1965**, *274*, 832–863.
- (10) Pope, J. M.; Buttry, D. A. Measurements of the potential dependence of electric field magnitudes at an electrode using fluorescent probes in a self-assembled monolayer. *J. Electroanal. Chem.* **2001**, *498*, 75–86.
- (11) Oklejas, V.; Sjostrom, C.; Harris, J. M. SERS detection of the vibrational Stark effect from nitrile-terminated SAMs to probe electric fields in the diffuse double-layer. *J. Am. Chem. Soc.* **2002**, *124*, 2408–2409.
- (12) Eggers, P. K.; Darwish, N.; Paddon-Row, M. N.; Gooding, J. J. Surface-bound molecular rulers for probing the electrical double layer. *J. Am. Chem. Soc.* **2012**, *134*, 7539–44.
- (13) Favaro, M.; Jeong, B.; Ross, P. N.; Yano, J.; Hussain, Z.; Liu, Z.; Crumlin, E. J. Unravelling the electrochemical double layer by direct probing of the solid/liquid interface. *Nat. Commun.* **2016**, *7*, 12695.
- (14) Pope, J. M.; Tan, Z.; Kimbrell, S.; Buttry, D. A. Measurement of electric fields at rough metal surfaces by electrochromism of fluorescent probe molecules embedded in self-assembled monolayers. *J. Am. Chem. Soc.* **1992**, *114*, 10085–10086.
- (15) Smith, C. P.; White, H. S. Theory of the interfacial potential distribution and reversible voltammetric response of electrodes coated with electroactive molecular films. *Anal. Chem.* **1992**, *64*, 2398–405.
- (16) Rentsch, S.; Siegenthaler, H.; Papastavrou, G. Diffuse layer properties of thiol-modified gold electrodes probed by direct force measurements. *Langmuir* **2007**, *23*, 9083–9091.
- (17) Chen, A. C.; Lipkowski, J. Electrochemical and spectroscopic studies of hydroxide adsorption at the Au(111) electrode. *J. Phys. Chem. B* **1999**, *103*, 682–691.
- (18) Ozaki, Y.; Tanabe, I. Far-ultraviolet spectroscopy of solid and liquid states: characteristics, instrumentation, and applications. *Analyst* **2016**, *141*, 3962–3981.
- (19) Chen, T.; Wang, D.; Gan, L. H.; Matsuo, Y.; Gu, J. Y.; Yan, H. J.; Nakamura, E.; Wan, L. J. Direct probing of the structure and electron transfer of fullerene/ferrocene hybrid on Au(111) electrodes by in situ electrochemical STM. *J. Am. Chem. Soc.* **2014**, *136*, 3184–3191.
- (20) Kotani, H.; Ohkubo, K.; Takai, Y.; Fukuzumi, S. Viologen-modified platinum clusters acting as an efficient catalyst in photocatalytic hydrogen evolution. *J. Phys. Chem. B* **2006**, *110*, 24047–24053.
- (21) Liu, B.; Blaszczyk, A.; Mayor, M.; Wandlowski, T. Redox-switching in a viologen-type adlayer: an electrochemical shell-isolated

nanoparticle enhanced Raman spectroscopy study on Au(111)-(1 × 1) single crystal electrodes. *ACS Nano* **2011**, *5*, 5662–5672.

(22) De Long, H. C.; Buttry, D. A. Environmental effects on redox potentials of viologen groups embedded in electroactive self-assembled monolayers. *Langmuir* **1992**, *8*, 2491–2496.

(23) Miano, F.; Rabaioli, M. R. Rheological scaling of montmorillonite suspensions: the effect of electrolytes and polyelectrolytes. *Colloids Surf., A* **1994**, *84*, 229–237.

(24) Osorio, H. M.; Martin, S.; Milan, D. C.; Gonzalez-Orive, A.; Gluyas, J. B. G.; Higgins, S. J.; Low, P. J.; Nichols, R. J.; Cea, P. Influence of surface coverage on the formation of 4,4'-bipyridinium (viologen) single molecular junctions. *J. Mater. Chem. C* **2017**, *5*, 11717–11723.

(25) Ulman, A. Formation and structure of self-assembled monolayers. *Chem. Rev.* **1996**, *96*, 1533–1554.

(26) Tansel, B.; Sager, J.; Rector, T.; Garland, J.; Strayer, R. F.; Levine, L.; Roberts, M.; Hummerick, M.; Bauer, J. Significance of hydrated radius and hydration shells on ionic permeability during nanofiltration in dead end and cross flow modes. *Sep. Purif. Technol.* **2006**, *51*, 40–47.

(27) Marcus, Y. Thermodynamics of solvation of ions. Part 5.—Gibbs free energy of hydration at 298.15 K. *J. Chem. Soc., Faraday Trans.* **1991**, *87*, 2995–2999.

(28) Zhou, J.; Lu, X. H.; Wang, Y. R.; Shi, J. Molecular dynamics study on ionic hydration. *Fluid Phase Equilib.* **2002**, *194*, 257–270.